IEEE Robotics and Automation Letters (RA-L) paper, presented at ICRA 2026, Vienna, Austria. Cite as RA-L paper.

A Piezoelectrically-Actuated Mesoscale Compliant Parallel Robot via Additive Manufacture

Ariel Tabak[1], Annamalai Karuppiah[1], and Ryan Orszulik[1]

***Abstract*—Micro-positioning and pick-and-place applications at the millimeter scale are driving the development of smaller robots necessitating the use of alternative methods for design and manufacture. Additive manufacturing can enable significant cost and time savings in the fabrication of robots while having a low barrier to entry. Specifically, multimaterial 3D printing naturally lends itself to the creation of monolithic mechanisms by removing the requirement for manual assembly, in particular, when compliant joints can replace the rigid joints that are traditionally used. The lack of an assembly requirement naturally opens up the possibility of reducing the size scale of these mechanisms. In this work, the design, fabrication, and characterization of an additively manufactured mesoscale compliant parallel robot actuated by piezoelectric bimorphs through a compliant transmission mechanism is presented. The transmission mechanism is required to convert and amplify the small but rapid linear displacements of piezoelectric actuators into the large rotational motion that is required to create a large workspace for the compliant parallel robot. The developed planar parallel robot has a workspace with maximum planar extents of 14.36 mm by 8.66 mm, with a total area of 65.6 mm^2. Three different trajectories are tracked at frequencies of up to 10 Hz, demonstrating the robot's capability to rapidly follow trajectories in its workspace.**

***Index Terms*—Additive Manufacturing, Compliant Joints and Mechanisms, Parallel Robots, Piezoelectric Actuation.**

I. Introduction

MESOSCALE robotics is a growing area of research bridging the gap between macroscale and microscale robots, in particular for applications including surgery, micropositioning, pick-and-place, and microassembly [1]. The design, fabrication, and assembly of these robots, however, can be challenging due to the difficulties of manufacturing at the millimeter to centimeter scale [2], [3]. Macroscale manufacturing has challenges due to the minimum feature sizes required, which limits the effectiveness of machining and other standard macro-manufacturing methods [4]. Conversely, micromanufacturing methods used for micro-electromechanical systems are often planar, leading to increased design complexity and fabrication time for larger three-dimensional structures [5], [6]. To overcome these challenges, new manufacturing methods have been developed, such as printed circuit microelectromechanical systems (PC-MEMS), which use origami-inspired designs in conjunction with multimaterial laminates [7], [8]. These methods have been shown to be capable of producing a variety of millimeter-scale robots, including delta robots [9], remote center-of-motion manipulators [10], and flying robots [11]. Due to the pop-up design and the number of manufacturing steps required, modifying the design of these mechanisms can result in numerous changes during manufacturing [12]. The development of additive manufacturing opens up a new avenue for the fabrication of millimeter-scale mechanisms, where parts are formed layer by layer [13]. Additive manufacturing processes allow for the simultaneous fabrication of multiple designs, monolithic fabrication, minimal post-processing, and a reduction in the length of each design cycle. A variety of additive manufacturing processes are available, including photo-polymerization, material extrusion, and powder bed fusion [14]. Material jetting 3D printers use inkjet print heads to deposit and cure photo-polymer resins and are capable of producing parts using multiple materials, allowing for rigid and flexible materials to be integrated in the same part [15]. With a low barrier to entry, this process is an affordable fabrication method that does not require significant pre-requisite knowledge. For the fabrication of robotic mechanisms, additive manufacturing has been investigated as a method to print smart structures directly [16], through the use of technologies such as pattern magnetization [17], shape-memory polymers [18], and direct printing of piezoelectric materials [19]. Additive manufacturing has been used to fabricate mesoscale mechanisms that take advantage of a compliant design such as delta robots [20], grippers [21], [22], and soft actuators [23]. The use of compliant mechanisms makes additive manufacturing a desirable choice [24], where multimaterial printing methods can be used to print rigid and flexible regions of a single part simultaneously [25].

The actuation of mesoscale robots also comes with its own challenges, in particular when scaling down commonly used actuators such as rotary motors, due to the impact of surface forces such as friction [26], [27], [28]. To overcome this, actuators such as piezoelectric bimorphs [29] , voice coil actuators [30] , and shape memory actuators [31] have been investigated to serve as alternative options for mesoscale robotics. Of these, piezoelectric actuators are frequently used due to their precise high-speed linear displacement, large blocking force, and small size [32]. The displacement for many piezoelectric bimorphs is in the sub-millimeter range, however, and must be amplified to be used effectively. Other mesoscale robots have used linkage mechanisms such as four-bar linkages [11], [33] and linkages combined with flexible joints and crank sliders [9] to accomplish this motion amplification.

Manuscript received: July 25, 2025; Revised October 10, 2025; Accepted November 9, 2025 .

This paper was recommended for publication by Editor Clement Gosselin upon evaluation of the Associate Editor and Reviewers' comments. This work was supported by an NSERC Discovery Grant.

[1]The authors are with the Department of Earth and Space Science and Engineering, Lassonde School of Engineering, York University, Toronto, Canada, M3J 1P3. ryan.orszulik@lassonde.yorku.ca

Digital Object Identifier (DOI): see top of this page.

IEEE Robotics and Automation Letters (RA-L) paper, presented at ICRA 2026, Vienna, Austria. Cite as RA-L paper.

This work presents a compliant mesoscale parallel robot driven by piezoelectric actuators that takes advantage of multimaterial additive manufacturing for monolithic design to reduce the barrier to entry for the creation of small-scale robots. A linear-to-rotary conversion mechanism is used to convert and amplify the displacement of a piezoelectric actuator into a large rotational motion [34]. Compliant mechanisms transfer the motion of the piezoelectric bimorph directly through the use of flexure joints that allow for the typically rigid connections to be replaced with flexible members that can achieve similar motion to revolute joints while eliminating friction [35]. The rotational motion from the transmission mechanism serves as the basis of the actuation for the parallel robot, which is additively manufactured using multimaterial jetting print technology. It is shown that the use of multimaterial printing is critical for the motion of the transmission. The use of this manufacturing process allows for various designs to be fabricated concurrently, and post-processing is simple, consisting solely of support removal. A design can be finalized, fabricated, assembled, and tested within a few hours. In this work, a 2RRR (or six-bar) parallel robot design is investigated that utilizes piezoelectric bimorphs and a compliant linear-to-rotary transmission mechanism for actuation. Two 3R chains are combined with an end effector to form a 2RRR parallel robot as shown in Fig. 1. This parallel robot has three degrees of freedom (movement along the x-axis, movement along the y-axis, and the orientation ϕ of the end effector), but only two actuators, making it underactuated, where the orientation of the end effector cannot be independently controlled at a given position (x, y). This is due to the flexure-based nature of the parallel robot design necessitating a rigid link at the location of the end effector, however, the orientation of the end effector is limited to departures of less than eight degrees (which is seen as sufficiently small given the compliance of the robot and as a demonstration of pick-and-place tasks). In Fig. 1a the transmission mechanism is depicted (as a simplification) as an active revolute joint (A_t, A_b), while the joints between rigid links (l_{1t}, l_{2t}, l_{1b}, l_{2b}) and the end effector (E) are depicted as passive revolute joints (P_{1t}, P_{2t}, P_{1b}, P_{2b}). The 2RRR parallel robot is shown experimentally to have a workspace area of 65.6 mm^2, while covering an area of 558 mm^2, resulting in the workspace being nearly 12% of the total robot's structural area. This workspace is optimized via finite element analysis where it is shown that the multimaterial composition of the robot is critical. The performance of the robot is demonstrated experimentally by following three different trajectories at varying frequencies of up to 10 Hz with good precision. It is also shown based on the frequency response of the structure that tracking of trajectories at up to 30 Hz is possible. These speeds enable applications in high-speed manipulation and assembly of millimeter-scale components, while the manufacture using commercially available additive printing technology allows for the robots to be custom designed for specific applications with ease. The contributions of this paper are i) the design of a multimaterial transmission and parallel robot for additive manufacture, ii) analysis of the achievable amplification of the transmission and workspace of the parallel robot considering rigid, flexible, and multimaterial (rigid+flexible) compliant designs, iii) the additively manufacture and validation of a piezoelectrically-driven compliant parallel robot, that must only be attached to its actuators and requires no other manual assembly.

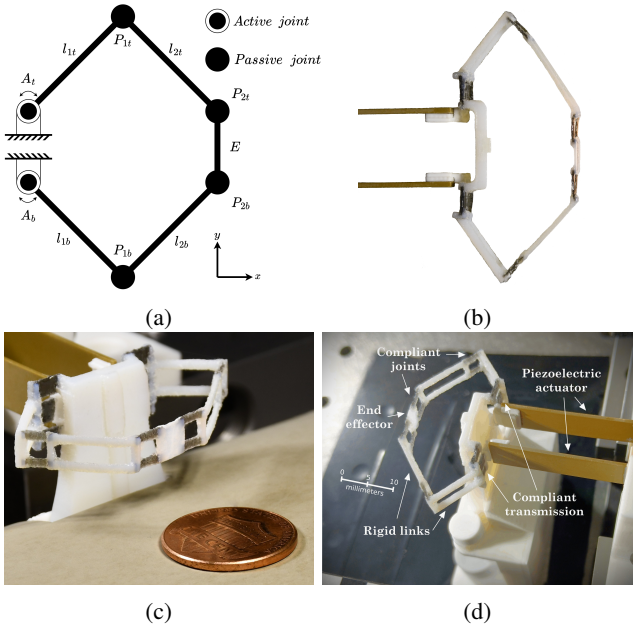

Fig. 1: (a) Schematic of the parallel robot depicting the links and joints. (b) Top view of the printed compliant parallel robot. (c) Side view with US penny for scale and (d) labelled components of the parallel robot.

II. Actuation and Compliant Transmission

Piezoelectric bimorph actuators are favorable for actuation at small scales due to their relatively precise displacements and high bandwidth. Their compact shape and overall size make them easy to integrate with other components. For this work the Thorlabs PB4NB2W piezoelectric bender is selected, presenting an inexpensive and commercially available option for mesoscale actuation. To determine the experimental performance of the Thorlabs PB4NB2W benders, four benders are tested to determine peak displacements and resonance frequencies as seen in Fig. 2. Actuators A and C are seen to have peak displacements of 380.35 and 401.5 µm at 1 Hz and resonances at frequencies of 374.4 and C 366.5 Hz and are therefore selected for use.

A. Transmission

To create a large workspace for the parallel robot, a transmission mechanism is required to convert and amplify the small linear motion of a piezoelectric bimorph to a large rotational motion. The design of the transmission mechanism can be seen in Fig. 3a and is similar to other linearizing transmission designs [9], [36]. However, this transmission mechanism makes use of much longer flexures than are commonly employed in compliant mechanisms and the design is simplified for 3D printing where the offset between the driven and

IEEE Robotics and Automation Letters (RA-L) paper, presented at ICRA 2026, Vienna, Austria. Cite as RA-L paper.

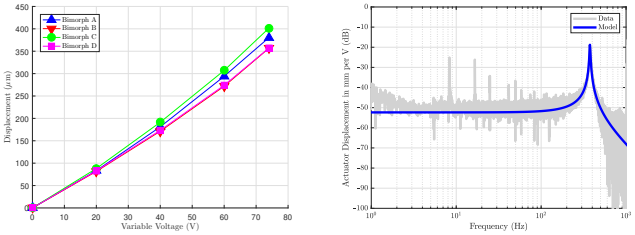

(a) (b)

Fig. 2: (a) Peak displacements of the four actuators against the applied voltage. (b) The experimental and modeled frequency response of actuator A.

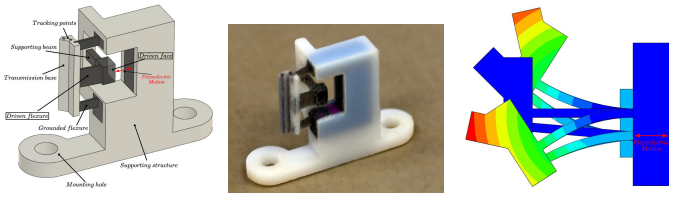

(a) (b) (c)

Fig. 3: (a) Schematic of the transmission mechanism with material encasement and points for tracking of the motion. (b) The printed multimaterial transmission. (c) Simulated motion of the flexure-based transmission for converting linear motion into rotational motion.

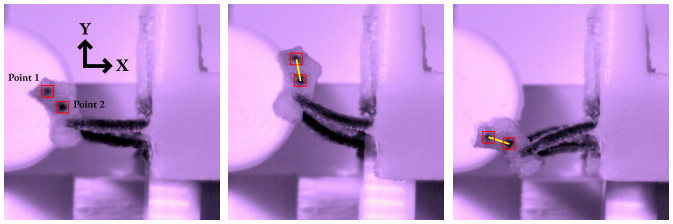

(a) (b) (c)

Fig. 4: Experimental results for the transmission. (a) The neutral position of the transmission with points for image processing indicated. (b) Transmission rotation in the clockwise (negative) direction and (c) counter-clockwise (positive) direction.

grounded flexures is small but the driven flexure (see Fig. 3c) is at a small relative angle to that of the grounded flexures. This design simplifies fabrication while yielding a nearly linear relation across the range of inputs the piezoelectric actuator is capable of producing. Preliminary designs of this transmission mechanism have been examined and additively manufactured using flexible material only [34]. In this work, the transmission is revised and a multimaterial design is investigated with an improved experimental setup. Two transmission designs are considered, where the first consists of a transmission that is composed of only flexible material, while the second employs both rigid and flexible materials, as seen in Fig. 3b. The flexible material for the transmission is Agilus30 Black, a rubber-like material, and the rigid material is VeroWhite, a common choice for rigid materials in Stratasys PolyJet systems. Both of these materials are photopolymers produced by Stratasys. VeroWhite is taken to have a modulus of elasticity of 2.5 GPa and a Poisson's ratio of 0.33 [37] while Agilus30 Black has a modulus of elasticity of 3.0 MPa and Poisson's ratio of 0.45 [38] [39], although it is known that the Agilus30 Black material will exhibit viscoelastic behaviour that is common for elastomeric materials. Hence it can be seen that the two materials have a nearly three orders of magnitude difference in their stiffnesses and that the Agilus30 is nearly incompressible. Multimaterial printing allows for the mount of the transmission mechanism to be rigid, rather than flexible, ensuring that the force applied to the transmission mechanism and resulting stresses remain in the desired regions to create motion. The material boundary between the flexible material and the rigid material is an area of concern, as this region is susceptible to separation due to the small area connecting these regions. To overcome this issue, a portion of the flexible material is enclosed within the rigid material, such that the region of the flexures experiencing the largest stress is not at the interface between the two materials as shown in Fig. 3a and Fig. 4.

The grounded flexures have dimensions of 3.5 mm in length, 1.5 mm in width, and 0.392 mm in thickness while the driven flexure has the same dimensions with the exception of a 3 mm width and a 5° relative angle to that of the grounded flexures. These parameters are selected by stepping piecewise across the FE model domain until the transmission rotation is at least 25° and the parameters are feasible for manufacture. In addition, as printing errors or other deviations in the final printed part can have a significant impact on the performance of the mechanism, the offset between the flexures of the transmission is chosen to be 0.5 millimeters. For tracking and visual processing of data, two points of contrasting material are added (shown in Fig. 3a) to the transmission base that connects the flexures. Finally, a supporting beam is added to the transmission for alignment during assembly (shown in Fig. 3b). This supporting beam is composed of flexible material and is cut off once the transmission mechanism has been mounted and the initial position has been obtained.

B. Experiments

To verify the performance of the transmission designs (see Fig. 3b) and compare the designs to the developed finite element models, the transmission is first connected to a 3D-printed optical table mount. A flexure driver (a rigid beam acting as a replacement for the piezoelectric actuators) is connected to a Thorlabs NRT100M linear motorized stage with a Thorlabs BSC201 controller, allowing for precise control over the driven flexure displacement. The flexure driver is then positioned to be in contact with the driven flexure of the transmission mechanism. Once the flexure driver is glued to the driven flexure of the transmission mechanism, the supporting beam is cut and removed. At this stage (shown in Fig. 4a and 5a), the transmission mechanism is in the neutral position and is ready for testing.

To determine the rotation of the transmission mechanism, two points are marked on the angled bar of the transmission

IEEE Robotics and Automation Letters (RA-L) paper, presented at ICRA 2026, Vienna, Austria. Cite as RA-L paper.

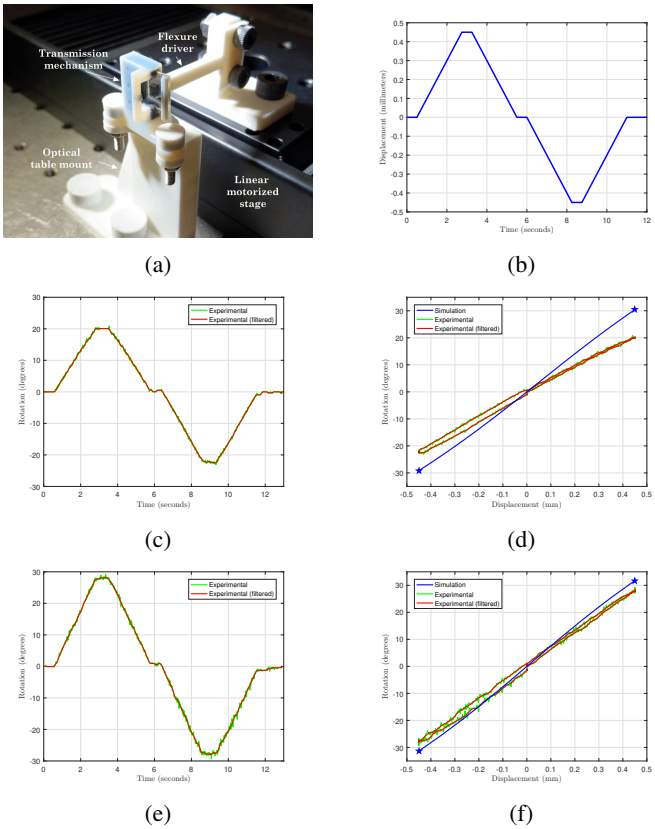

Fig. 5: (a) Experimental setup for testing of the transmission mechanisms. (b) Trapezoidal waveform input to the motorized stage with measured rotational motion of the flexible only transmission (c) and the multimaterial transmission (e). Depiction of the linear input displacement versus output rotation of the transmission for experimental and finite element model for the flexible only (d) and multimaterial (f) transmission.

base (shown in Fig. 4a) and a Chronos 2.1 high-speed camera is positioned above to record the movement at 1000 frames per second as the transmission is actuated. Motion tracking software (ProAnalyst) is used to determine the displacement of each point, frame by frame. To determine the rotation of the transmission mechanism, a vector is defined between the contrasting points. This vector is calculated at each frame and compared to the vector of the transmission mechanism at rest by taking the dot product of the vectors to obtain the rotation. Due to the resolution of the video data, small jumps in the results appear as the tracking software attempts to track points that are only pixels across. To account for this, a ten-point moving average filter is employed. To actuate the transmission mechanism, the linear motorized stage uses a trapezoidal waveform (shown in Fig. 5b). Displacement in the positive direction corresponds to a counter-clockwise (positive) rotation in the transmission mechanism, whereas displacement in the negative direction corresponds to a clockwise (negative) rotation.

From the results seen in Fig. 5d and Fig. 5f, there is a clear difference in the performance of the transmission consisting of only flexible materials to that of the transmission that uses both rigid and flexible materials. The multimaterial transmission had a simulated peak rotation of 31.29 degrees clockwise and 31.81 degrees counter-clockwise, with an experimental peak rotation of 29.35 degrees clockwise and 29.19 degrees counter-clockwise. The flexible-only transmission had a simulated peak rotation of 30.44 degrees clockwise and 29.38 degrees counter-clockwise with an experimental peak rotation of 23.08 degrees clockwise and 20.93 degrees counter-clockwise. Between the two, the multimaterial base has a higher peak rotation and a narrower hysteresis loop compared to the base composed of only flexible material. The discrepancy seen between the model and experimental values for the transmission printed in only flexible material, seen in Fig. 5d, is due to imperfect fixation of the grounded flexures in the experiment. The finite element model considers only the transmission itself with the grounded flexures being perfectly constrained, however in the experiment, parasitic motion of the mount is seen due it being fully printed from a flexible material and thus not being stiff enough to prevent deflection. For the multimaterial transmission the results appear to be noisier due to the rigidity of the rigid material transmitting vibrations from the linear stage. Further improvements to the positional accuracy during integration would allow for the performance of the transmission mechanism to be improved. Between the two designs tested, the transmission mechanism using multiple materials is chosen for implementation in the parallel robot due to the narrower hysteresis loop and larger peak rotation. The use of multimaterial additive manufacturing allows for multiple unique designs to be fabricated simultaneously without an increase in manufacturing complexity.

III. Parallel Robot Design

A kinematic model of the mechanism gives insight into how the parallel robot behaves and is useful to identify initial parameters but neglects the weight of the rigid bars and the behaviour of the flexures as these will experience significant bending in reality and are not truly pin joints. Thus, the flexures must be more accurately modeled to predict the performance of this parallel robot, hence a finite element model is required.

A. Finite Element Model

A finite element model of the parallel robot is implemented in ABAQUS to simulate the performance and optimize the design to maximize workspace, which naturally represents a tradeoff against frequency given the compliant nature of the joints. The model of the parallel robot is created through the use of reduced integration hexahedral (20-noded) elements throughout, with standard elements for the rigid members (C3D20R), piezoelectric elements (C3D20RE) for the actuators, and hybrid elements (C3D20RH) for the flexible joints to model the nearly incompressible behavior of the material. The force of gravity is included in the model along the z-axis to realistically model the physical environment. The piezoelectric bimorphs used in the parallel robot have lower displacements than specified, at approximately $375 - 400$ microns instead of 450 microns. The displacement at peak for the piezoelectrics is limited to 400 microns by lowering the peak voltage from

IEEE Robotics and Automation Letters (RA-L) paper, presented at ICRA 2026, Vienna, Austria. Cite as RA-L paper.

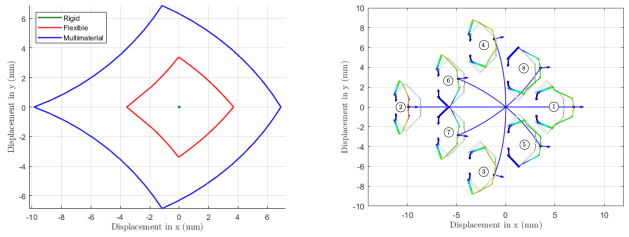

(a) (b)

Fig. 6: (a) Comparison of parallel robot workspaces with a single rigid material, single flexible material, and multimaterial (rigid+flexible) design. (b) Workspace of the parallel robot with the angle of end effector and deformation depicted for eight basic motions.

75 to 65 V in the finite element simulations. A significant deflection along the z-axis (parallel to the gravity vector) of 0.845 millimeters due to gravity was seen in initial models.

To reduce the deflection due to gravity, the design was optimized via iteration to reduce this deflection to less than 5% of the horizontal workspace of the robot, while maintaining a horizontal workspace of at least 15 millimeters. The optimization of the workspace is naturally a tradeoff against frequency, however the design is optimized for a larger workspace as this is in general more challenging to achieve with compliant parallel robots. The final design of the parallel robot encases the ends of all flexures and increases the thickness of the rigid arms, which were the most common feature to experience failure. The flexures in the transmission mechanism are increased to a thickness of 504 microns to reduce the deflection seen at the end effector. This resulted in a reduction of the actuated angle of the transmission to 27.1 degrees clockwise and 27.4 degrees counterclockwise. The workspace for the multimaterial parallel robot is shown in Fig. 6b where the total planar motion capabilities are 16.78 mm in x and 13.75 mm in y.

To illustrate the importance of the multimaterial design, three different workspaces are depicted in Fig. 6a. Here, the robot workspace with a single rigid material, a single flexible material, and the robot with multiple materials (rigid+flexible) can be seen. The rigid-only robot design, unsurprisingly has effectively zero workspace as the piezoelectrics are unable to generate enough force to produce motion, even with the extremely thin flexure regions. The flexible-only design shows a reasonable workspace, however, it is only approximately 20% of that of the multimaterial design. This is primarily for two reasons, the first being that bending is not localized at the flexure joints, as all of the links tend to deform slightly, even when their structure is modified to try to prevent this deformation. The second is that the transmission is simply not as effective in the flexible-only design, resulting in a smaller amplified motion from the actuators to begin with.

B. Fabrication

Fabrication is performed using a Stratasys Objet Connex500 PolyJet printer. As the thickness of the flexures is critical to the performance of the transmission, the parallel robot is printed with the flexure thickness direction aligned perpendicular to the plane of the print tray, ensuring the flexures are printed as precisely as possible through the thickness. Once the support material is removed the robot is ready for use.

IV. Experiments

To prepare the parallel robot for experimental testing, the mechanically grounded flexures are connected and extended into a base with mounting holes to assist with setup. An Ultimaker S5 3D printer is used to print bimorph mounts from Tough PLA material that are connected to a micrometer stage. Each of the piezoelectric actuators are mounted on a micrometer stage (shown in Fig. 1d) and a rectangular section of non-conductive material is glued to the end of each bimorph, which is then glued to a connecter for the transmission of the parallel robot (which is shaped to cover the driven flexure cap of the transmission). The micrometer stage is used to adjust the position of the bimorphs as the bimorph connectors are glued to the robot transmissions and then the bimorphs are positioned such that the parallel robot is in a neutral position.

To test the parallel robot, each of the piezoelectric bimorph actuators is wired to a PiezoDrive PD200X4 four channel amplifier and driven in biased unipolar mode. The bias voltages for each bimorph are connected to the ground and high-voltage outputs of the amplifier while the first two independent outputs of the amplifier are connected to the control voltage of each of the first (top) and second (bottom) actuators and able to vary between the ground and high voltage bias. Both of these outputs from the amplifier are controlled via signals from Simulink using a Speedgoat Performance Real-Time machine with an IO133 module. To monitor the position of the parallel robot end effector, a Chronos 2.1 high-speed camera from Kron Technologies is positioned above the parallel robot to record motion as the robot is actuated. To extract the displacement of the end effector, a checkerboard pattern calibration image is placed at the same height as the end effector (shown in Fig. 1d). The motion tracking software ProAnalyst is used to track two separate points on the end effector giving both the location and orientation of the end effector in plane.

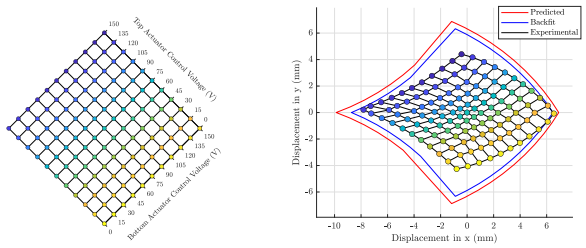

(a) (b)

Fig. 7: (a) Depiction of the set of control voltages applied to the piezoelectric actuators. (b) Model versus the workspace area found experimentally.

A. Workspace

As parallel robots typically have smaller workspaces than their serial counterparts, and flexure-based parallel robots less

IEEE Robotics and Automation Letters (RA-L) paper, presented at ICRA 2026, Vienna, Austria. Cite as RA-L paper.

than their rigid counterparts, the first experimental task is to determine the workspace of the robot. A grid of input voltages to the piezoelectric actuators is generated, as seen in Fig. 7a. These voltages are then applied three times in different sequences and the results averaged to compute the end effector position, shown in Fig. 7b, for a given combination of input voltages (with colors coordinated to represent the resulting displacement for a combination of applied voltages). This is done in order to mitigate the effect of actuator hysteresis as the actuators are run without closed-loop control. Compared to the finite element model, the workspace is smaller and more diamond-shaped due to a reduction in the motion in the y direction. The total stroke in x (the horizontal direction) is 14.36 millimeters (as compared to the characteristic length of the robot in the x-direction in its nominal configuration of 20.5 mm), and a total stroke in y (the vertical direction) of 8.66 millimeters (as compared to the maximum y-dimension of the robot of 38 mm). This results in the total area of the workspace being 65.6 mm^2 as compared to the total area of the parallel robot structure at 558 mm^2. While the difference in total stroke in the x-direction is relatively small as compared to the model, the difference in the total stroke in the y-direction is relatively large. As a result, the linear elastic modulus was fit to the transmission experiments and applied to create a fitted model. With the backfit model there is a small discrepancy in x, however the substantial error in y still exists. Hence, it is hypothesized that this is a result of the actuation. As the piezoelectric actuators are inverted on their mounts with respect to each other, when driving in or out along the x axis, they are driven identically from an electrical perspective. When the robot is moved in either direction in y, the actuators are being driven in opposite manners. Given that piezoelectric actuators have asymmetric hysteresis loops it is thought that this combination of inputs gives rise to the deviation seen in the achievable motion in the y-direction.

B. *Quasi-Static and Dynamic Performance*

As the piezoelectric actuators have first resonances on the order of approximately 360 Hz (Fig. 2b), and the robot itself possesses modeled resonances at approximately 18, 19, 28, and 115 Hz, three different trajectories are generated for the parallel robot to follow. These trajectories are generated at 0.5 Hz, to capture quasi-static performance, and at 2, 5, and 10 Hz to capture dynamic performance (see Video S1 to S3 attached as supplementary information).

To start, the first trajectory examined is that of the workspace itself (overlaid on the robot in Fig. 8a and shown in Fig. 8d). There are slight differences in the results that are visible near the lower half of the trace, which occurs later in the trajectory. Hysteresis in both the piezoelectric actuators and the material of the flexures is the likely source of this error, as the first half of the trajectory is more aligned with the workspace grid found earlier. At higher frequencies, seen in Fig. 8e it can be seen that the workspace of the robot shrinks slightly while path differences become more pronounced, indicating viscoelastic behaviour of the flexure joints.

The second trajectory examined is a circular trajectory with a radius of 3.5 mm centered at the neutral position of the

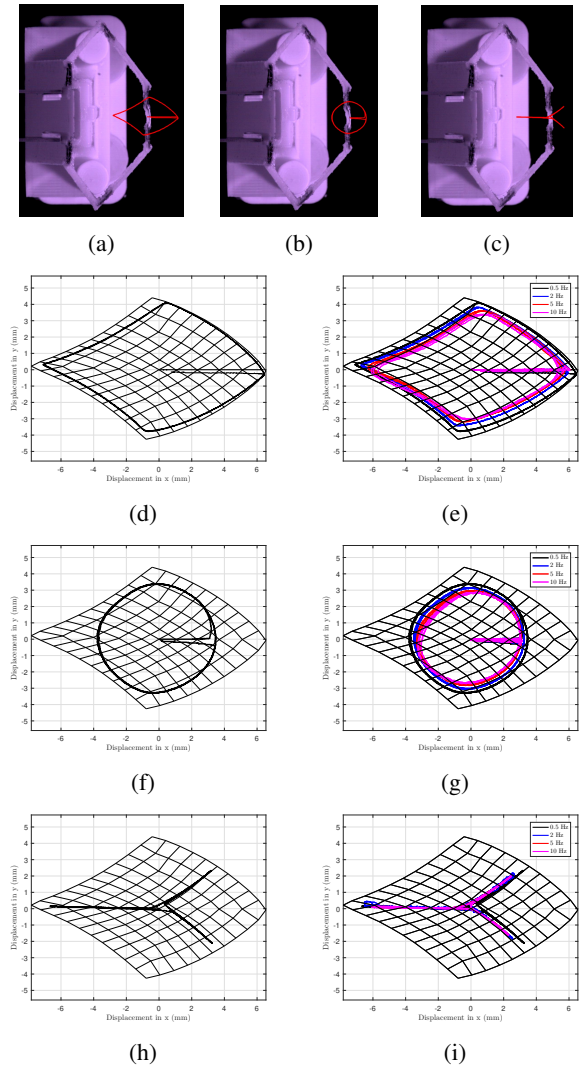

Fig. 8: Trajectory tracking results. Overlay of the trajectory traced for the quasi-static case seen for the workspace trajectory (a), circular trajectory (b), and Y trajectory (c). Results of the quasi-static trajectory tracking at 0.5 Hz for the workspace trajectory (d), circular trajectory (f), and Y trajectory (h). High-frequency trajectory tracking at 2, 5, and 10 Hz shown for the workspace trajectory (e), circular trajectory (g), and Y trajectory (i).

parallel robot. In the quasi-static case of Fig. 8b and 8f, the robot can be seen to accurately trace the trajectory, while at higher frequencies, at up to 10 Hz, the radius of the circle can be seen to diminish as shown in Fig. 8g along with the accuracy of the trace. Finally, a Y-trajectory is examined to see the robot performance for a trajectory containing three distinct linear components giving rise to areas that require large accelerations and decelerations. The trace of this trajectory is overlaid as can be seen in Fig. 8c. Hysteresis is clearly visible in Fig. 8h as the robot passes back through the neutral position. As the upper segment of the trajectory is traced, it does not return fully to the origin before beginning the lower segment of the trajectory and has a slightly different origin when returning to rest at the end. At higher frequencies (shown in Fig. 8i) the trajectory is

IEEE Robotics and Automation Letters (RA-L) paper, presented at ICRA 2026, Vienna, Austria. Cite as RA-L paper.

TABLE I: Precision and accuracy for each trajectory and frequency.

Trajectory	Cycle length [mm]	Freq. [Hz]	RMS Precision [mm]	RMS Accuracy [mm]
Workspace	33.9386	0.5	0.0408 ± 0.0136	0.6760 ± 0.0069
		2	0.0535 ± 0.0189	0.8845 ± 0.0203
		5	0.0922 ± 0.0348	0.9622 ± 0.0236
		10	0.1576 ± 0.0657	1.0173 ± 0.0475
Circle	21.9911	0.5	0.0490 ± 0.0138	0.2311 ± 0.0066
		2	0.0538 ± 0.0185	0.4316 ± 0.0134
		5	0.0623 ± 0.0226	0.6984 ± 0.1255
		10	0.0852 ± 0.0355	0.7319 ± 0.1169
Y	32.9842	0.5	0.0726 ± 0.0200	0.4911 ± 0.0161
		2	0.0521 ± 0.0110	0.6536 ± 0.0191
		5	0.0604 ± 0.0268	0.6386 ± 0.0228
		10	0.0504 ± 0.0186	0.7831 ± 0.0306

clearly traced, but the peak displacements are smaller.

For all of the trajectories, the accuracy and precision are tabulated in Table I. In general, it can be seen that the precision of the robot is best in the quasi-static case with a precision down to 40.8 ± 13.6 µm, with degradation at higher frequencies to 157.6 ± 65.7µm in the worst case. The accuracy is in general sub-millimeter, however as the robot is run without any control, the accuracy could be substantially improved by introducing closed-loop control of the piezoelectric actuators, by shaping the trajectories to minimize jerk (as the trajectories are currently evenly-spaced in time), inverting a dynamical model of the parallel robot for feedforward control, or introducing vision-based closed-loop control of the end-effector.

1) Frequency Response: To determine the frequency response of the parallel robot, a chirp signal with a magnitude of 15V is applied to each bimorph in separate experiments. The chirp signal lasts for five seconds, sweeping from 1 to 50 Hz and the position of the end effector is monitored via the high-speed camera. In ProAnalyst, the position in the two planar Cartesian directions is computed from the high-speed video. Fig. 9 shows the magnitude response of the 2×2 transfer function matrix $\mathbf{G}(j\omega)$. A continuous linear representation of the parallel robots dynamics are estimated via subspace methods with the voltages as input $\mathbf{u} = [V_1\ V_2]^T$ and the displacements as output $\mathbf{y} = [x\ y]^T$. From each actuator to the x-direction, it can be seen that there is a decrease in the response of the system as it increases from 1 to 5 Hz. This is likely due to the stiffness of the elastomer increasing with frequency. The response peaks around 25 Hz, before rolling off as the frequency increases further. The first three resonance frequencies predicted by the finite element model are 17.74, 18.82, and 27.58 Hz, however this is based on a linear material model. For the actuators to the y-direction, the system response does not change significantly from 1 to 5 Hz, but then begins to roll off without evidence of resonance. This does imply that with a controller for the parallel robot, much higher frequencies could be tracked reliably.

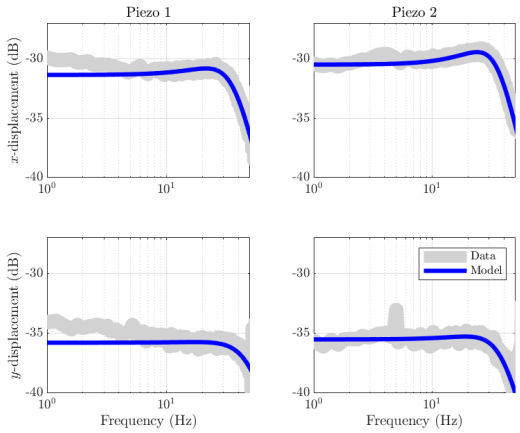

Fig. 9: Frequency response matrix from the voltage input to the piezoelectric actuators to the end effector motion in Cartesian directions.

V. Discussion and Future Work

In this work, a compliant mesoscale parallel robot was designed for additive manufacture via finite element for actuation via piezoelectric bimorphs. To achieve high-frequency motion, the use of piezoelectric actuators necessitated the development of a compliant transmission mechanism that converts small linear displacement into a large rotational motion. Experimental testing of the flexure-based mechanism demonstrated the transmission behaved as expected, with the multimaterial design enabled by additive manufacture being critical to the performance of the transmission. The transmission is then integrated with a compliant parallel robot structure to form a planar 2RRR parallel robot. A finite element model was developed that incorporated the piezoelectric bimorph and transmission mechanism models along with the properties of the rigid and flexible materials such that the workspace of the parallel robot was maximized.The robot was fabricated in a single step via multimaterial 3D printing based on this design, and experimental testing demonstrated that the workspace of the robot is relatively close to that of the model. The parallel robot has x and y motion capabilities of 14.36 and 8.66 millimeters, respectively, with a reduction to 12.06 and 6.80 millimeters, respectively, at 10 Hz. Trajectories spanning the entire workspace can be maintained at 10 Hz, while cyclical tests showed no change in performance after $10,000$ cycles. Higher frequencies are possible, however, this represents a tradeoff against the size of the workspace, which in this case was the objective for optimization.

There are a number of areas that require further investigation. To start, capturing the mechanical behavior of flexible materials, such as the material used in the flexures, at different strain rates and modeling the viscoelastic behavior accurately would allow for further design optimization of the parallel robot. This would also improve the modeling of the system at high frequencies and near resonance. Further, the actuators employed in this work do not employ closed-loop control which would improve performance at higher frequencies by accounting for hysteresis effects. On the parallel robot side, the trajectories could be shaped for example to minimize jerk, making the trajectories themselves more feasible for the robot to follow at the same rate. To account for the

IEEE Robotics and Automation Letters (RA-L) paper, presented at ICRA 2026, Vienna, Austria. Cite as RA-L paper.

hysteresis behavior of the bimorphs and flexible material in the transmission and improve both the precision and accuracy in tracking highly dynamic trajectories, vision-based closed-loop control of the end effector position could be enacted. Once the hysteresis of the actuators has been properly accounted for, comparisons of multiple parallel robots should be made to determine the effect of manufacturing variability on robot performance.

The transmission mechanism used for this parallel robot can be expanded to many other small-scale planar robot designs or spatial robots that can control the position and/or orientation of an end effector in three-dimensional space for a variety of micro-assembly or micro-positioning tasks. This design and fabrication strategy allows these robots to perform almost immediately after printing, providing a convenient process for creating task-specific robots that can simply be printed, cleaned, and connected to actuators.

REFERENCES

[1] P. Valdastri, R. J. Webster, C. Quaglia, M. Quirini, A. Menciassi, and P. Dario, "A new mechanism for mesoscale legged locomotion in compliant tubular environments," *IEEE Transactions on Robotics*, vol. 25, no. 5, pp. 1047–1057, 2009.

[2] I. Paprotny and S. Bergbreiter, "Small-scale robotics: An introduction," in *Workshop at the IEEE International Conference on Robotics and Automation*. Springer, 2013, pp. 1–15.

[3] P. S. Sreetharan, J. P. Whitney, M. D. Strauss, and R. J. Wood, "Monolithic fabrication of millimeter-scale machines," *Journal of Micromechanics and Microengineering*, vol. 22, no. 5, p. 055027, 2012.

[4] T. Dow and R. Scattergood, "Mesoscale and microscale manufacturing processes: Challenges for materials, fabrication and metrology," in *Proceedings of the ASPE Winter Topical Meeting*, vol. 28. ASPE, 2003, pp. 14–19.

[5] H. Hassanin, G. Sheikholeslami, P. Sareh, and R. B. Ishaq, "Microadditive manufacturing technologies of 3d microelectromechanical systems," *Advanced Engineering Materials*, vol. 23, no. 12, p. 2100422, 2021.

[6] S. Spearing, "Materials issues in microelectromechanical systems (MEMS)," *Acta Materialia*, vol. 48, no. 1, pp. 179–196, 2000.

[7] C. D. Onal, R. J. Wood, and D. Rus, "Towards printable robotics: Origami-inspired planar fabrication of three-dimensional mechanisms," in *2011 IEEE International Conference on Robotics and Automation*. IEEE, 2011, pp. 4608–4613.

[8] J. E. Correa, J. Toombs, N. Toombs, and P. M. Ferreira, "Laminated micro-machine: Design and fabrication of a flexure-based delta robot," *Journal of Manufacturing Processes*, vol. 24, pp. 370–375, 2016.

[9] H. McClintock, F. Z. Temel, N. Doshi, J. Koh, and R. J. Wood, "The millidelta: A high-bandwidth, high-precision, millimeter-scale delta robot," *Science Robotics*, vol. 3, no. 14, 2018.

[10] H. Suzuki and R. J. Wood, "Origami-inspired miniature manipulator for teleoperated microsurgery," *Nature Machine Intelligence*, vol. 2, no. 8, pp. 437–446, 2020.

[11] K. Y. Ma, P. Chirarattananon, S. B. Fuller, and R. J. Wood, "Controlled flight of a biologically inspired, insect-scale robot," *Science*, vol. 340, no. 6132, pp. 603–607, 2013.

[12] J. P. Whitney, P. S. Sreetharan, K. Y. Ma, and R. J. Wood, "Pop-up book MEMS," *Journal of Micromechanics and Microengineering*, vol. 21, no. 11, 2011.

[13] E. Sachyani Keneth, A. Kamyshny, M. Totaro, L. Beccai, and S. Magdassi, "3D printing materials for soft robotics," *Advanced Materials*, vol. 33, p. 202003387, 2021.

[14] T. J. Horn and O. L. Harrysson, "Overview of current additive manufacturing technologies and selected applications," *Science Progress*, vol. 95, no. 3, pp. 255–282, 2012.

[15] Y. L. Tee, C. Peng, P. Pille, M. Leary, and P. Tran, "Polyjet 3D printing of composite materials: experimental and modelling approach," *JOM*, vol. 72, pp. 1105–1117, 2020.

[16] J. Gardan, "Smart materials in additive manufacturing: state of the art and trends," *Virtual and Physical Prototyping*, vol. 14, no. 1, pp. 1–18, 2019.

[17] T. Xu, J. Zhang, M. Salehizadeh, O. Onaizah, and E. Diller, "Millimeter-scale flexible robots with programmable three-dimensional magnetization and motions," *Science Robotics*, vol. 4, no. 29, 2019.

[18] K. R. Ryan, M. P. Down, and C. E. Banks, "Future of additive manufacturing: Overview of 4d and 3d printed smart and advanced materials and their applications," *Chemical Engineering Journal*, vol. 403, p. 126162, 2021.

[19] C. Chen, X. Wang, Y. Wang, , F. Yao, W. Zhang, B. Wang, G. A. Sewvandi, D. Yang, and D. Hu, "Additive manufacturing of piezoelectric materials," *Advanced Functional Materials*, vol. 30, no. 52, p. 2005141, 2020.

[20] P. Mannam, O. Kroemer, and F. Z. Temel, "Characterization of compliant parallelogram links for 3D-printed delta manipulators," in *International Symposium on Experimental Robotics*. Springer, 2020, pp. 75–84.

[21] C. Tawk, A. Gillett, M. in het Panhuis, G. M. Spinks, and G. Alici, "A 3D-printed omni-purpose soft gripper," *IEEE Transactions on Robotics*, vol. 35, no. 5, pp. 1268–1275, 2019.

[22] C.-Y. Chen, B. W. Ang, Y. Li, J. Liu, Z. Liu, and C.-H. Yeow, "Soft printable robots with flexible metal endoskeleton," *IEEE Transactions on Robotics*, vol. 40, pp. 2907–2919, 2024.

[23] D. Drotman, S. Jadhav, M. Karimi, P. de Zonia, and M. T. Tolley, "3D printed soft actuators for a legged robot capable of navigating unstructured terrain," in *2017 IEEE International Conference on Robotics and Automation (ICRA)*. IEEE, 2017, pp. 5532–5538.

[24] N. A. Meisel, A. Gaynor, C. B. Williams, and J. K. Guest, "Multiple-material topology optimization of compliant mechanisms created via polyjet 3D printing," in *2013 International Solid Freeform Fabrication Symposium*. University of Texas at Austin, 2013.

[25] A. Bruyas, F. Geiskopf, L. Meylheuc, and P. Renaud, "Combining multi-material rapid prototyping and pseudo-rigid body modeling for a new compliant mechanism," in *2014 IEEE International Conference on Robotics and Automation (ICRA)*. IEEE, 2014, pp. 3390–3396.

[26] R. S. Fearing, "Powering 3 dimensional microrobots: Power density limitations," *Tutorial on Micro Mechatronics and Micro Robotics, ICRA*, vol. 98, 1998.

[27] W. S. Trimmer, "Microrobots and micromechanical systems," *Sensors and Actuators*, vol. 19, no. 3, pp. 267–287, 1989.

[28] S. T. Smith and R. M. Seugling, "Sensor and actuator considerations for precision, small machines," *Precision Engineering*, vol. 30, no. 3, pp. 245–264, 2006.

[29] N. T. Jafferis, M. J. Smith, and R. J. Wood, "Design and manufacturing rules for maximizing the performance of polycrystalline piezoelectric bending actuators," *Smart Materials and Structures*, vol. 24, no. 6, p. 065023, 2015.

[30] B. Goldberg, M. Karpelson, O. Ozcan, and R. J. Wood, "Planar fabrication of a mesoscale voice coil actuator," in *2014 IEEE International Conference on Robotics and Automation (ICRA)*. IEEE, 2014, pp. 6319–6325.

[31] J. Sheng, D. Gandhi, R. Gullapalli, J. M. Simard, and J. P. Desai, "Development of a meso-scale SMA-based torsion actuator for image-guided procedures," *IEEE Transactions on Robotics*, vol. 33, no. 1, pp. 240–248, 2016.

[32] C. D. Near, "Piezoelectric actuator technology," in *Smart Structures and Materials 1996: Smart Structures and Integrated Systems*, vol. 2717. International Society for Optics and Photonics, 1996, pp. 246–258.

[33] A. T. Baisch and R. J. Wood, "Design and fabrication of the harvard ambulatory micro-robot," in *Robotics Research: The 14th International Symposium ISRR*. Springer, 2011, pp. 715–730.

[34] A. Tabak and R. Orszulik, "A monolithic flexible transmission for piezoelectric actuators," in *2022 IEEE/ASME International Conference on Advanced Intelligent Mechatronics (AIM)*. IEEE, 2022, pp. 138–143.

[35] B. P. Trease, Y.-M. Moon, and S. Kota, "Design of large-displacement compliant joints," *Journal of Mechanical Design*, vol. 127, no. 4, pp. 788–798, 2005.

[36] W. Bachta, P. Renaud, E. Laroche, and J. Gangloff, "The cardiolock project: Design of an active stabilizer for cardiac surgery," *Journal of Mechanical Design*, vol. 133, no. 7, 07 2011.

[37] *Vero*, Stratasys Ltd., 2020. [Online]. Available: https://www.stratasys.com/siteassets/materials/materials-catalog/polyjet-materials/verovivid/mds_pj_vero_1020a.pdf

[38] *Agilus30*, Stratasys Ltd., 2022. [Online]. Available: https://www.stratasys.com/contentassets/1e715cc6ffe641cd9415e9631c17e192/mds_pj_agilus30_cmy_a4_1122a.pdf?v=4ab3d5

[39] D. M. Dykstra, J. Busink, B. Ennis, and C. Coulais, "Viscoelastic snapping metamaterials," *Journal of Applied Mechanics*, vol. 86, no. 111012, 2019.